Zonal Intratumoral Delivery of Nanoparticles Guided by Surface Functionalization

# Zonal Intratumoral Delivery of Nanoparticles Guided by Surface Functionalization

*Rossana Terracciano,[1,2] Yareli Carcamo-Bahena,[1] Amber Lee R. Royal,[1] Luca Messina,[3] Jack Delk,[4] E. Brian Butler,[5] Danilo Demarchi,[2] Alessandro Grattoni,[1,5,6] Zhihui Wang,[7,8,9] Vittorio Cristini,[7,8,10] Prashant Dogra,[7,9] and Carly S. Filgueira,[1,11*]*

[1]Department of Nanomedicine, Houston Methodist Research Institute, Houston, TX 77030, USA

[2]Department of Electronics and Telecommunications, Politecnico di Torino, Torino 10129, Italy

[3]Univestià degli Studi di Napoli Federico II, Naples 80138, Italy

[4]Texas A&M University, College Station, TX 77843, USA

[5]Department of Radiation Oncology, Houston Methodist Research Institute, Houston, TX 77030, USA

[6]Department of Surgery, Houston Methodist Research Institute, Houston, TX 77030, USA

[7]Mathematics in Medicine Program, Houston Methodist Research Institute, Houston, TX 77030, USA

[8]Department of Imaging Physics, University of Texas MD Anderson Cancer Center, Houston, TX 77030, USA

[9]Department of Physiology and Biophysics, Weill Cornell Medical College, New York, NY 10022, USA

[10]Physiology, Biophysics, and Systems Biology Program, Graduate School of Medical Sciences, Weill Cornell Medicine, New York, NY 10022, USA

[11]Department of Cardiovascular Surgery, Houston Methodist Research Institute, Houston, TX 77030, USA

***Corresponding author**: csfilgueira@houstonmethodist.org; Tel.: +1 713-441-1996

KEYWORDS: Zonal Accumulation, Intratumoral Transport, Gold Nanoparticles, Cytotoxicity, ICP-OES, Tumor Biodistribution, Mathematical Modeling, Agent-based Modeling

ABSTRACT. Delivery of small molecules and anticancer agents to malignant cells or specific regions within a tumor is limited by penetration depth and poor spatial drug distribution, hindering anticancer efficacy. Herein, we demonstrate control over Gold Nanoparticle (GNP) penetration and spatial distribution across solid tumors by administering GNPs with different surface chemistries at a constant injection rate via syringe pump. A key finding in this study is the discovery of different zone-specific accumulation patterns of intratumorally injected nanoparticles dependent on surface functionalization. Computed tomography (CT) imaging performed in vivo of C57BL/6 mice harboring Lewis lung carcinoma (LLC) tumors on their

**Commented [TR1]:** Limit 250 words, no claims of novelty, no structured, succinct, conclusive and informative summation of the most important result.

flank and gross visualization of excised tumors consistently revealed that intratumorally administered citrate-GNPs accumulate in particle clusters in central areas of the tumor, while GNPs functionalized with thiolated phosphothioethanol (PTE-GNPs) and thiolated polyethylene glycol (PEG-GNPs) regularly accumulate in the tumor periphery. Further, PEG functionalization resulted in larger tumoral surface coverage than PTE reaching beyond the outer zone of the tumor mass and into the surrounding stroma. To understand the dissimilarities in spatiotemporal evolution across the different GNP surface chemistries, we modeled their intratumoral transport with reaction-diffusion equations. Our results suggest that GNP surface passivation affects nanoparticle reactivity with the tumor microenvironment, leading to differential transport behavior across tumor zones. The present study provides a mechanistic understanding of the factors affecting spatiotemporal distribution of nanoparticles in the tumor. Our proof of concept of zonal delivery within the tumor may prove useful for directing anticancer therapies to regions of biomarker overexpression.

## INTRODUCTION

Overcoming challenges associated with therapeutic and nanoparticle tumor uptake and tissue penetration is critical for establishing effective cancer therapies. Accompanying systemic administration, challenges include off-target effects and associated toxicities. Intratumoral delivery has emerged as a means to enhance delivery locally and directly into the

**Commented [TR2]:** No more than 1000 words

**Commented [GA3]:** In my view, your intro should be structured as follows:

1. Intratumoral delivery as a mean to enhance delivery at the tumor with respect to systemic delivery. Much research is ongoing in this field…
2. TME heterogeneity still creates challenges in homogeneous distribution of therapeutics
3. Here we showed the ability to spatially control delivery of intratumorally injected GNP (zonal delivery) by leveraging different surface chemistry.
4. Further, by modelling… we elucidate the mechanistic aspects of the zonal delivery, which is determined by…
5. These exciting results provide a foundation for the development of …

tumor microenvironment (TME), thereby limiting systemic toxicity while permitting lower dosages.[1–3] Significant research is dedicated toward enhancing delivery to the TME and bypassing systemic administration, yet reproducible means to target zones within the TME itself have not been identified. As the TME is notoriously heterogeneous, this creates challenges in homogeneous therapeutic distribution. Current strategies to enhance nanoparticle diffusion into tissue with abnormal vasculature, such as solid tumors, include increasing vasculature permeability through approaches such as preconditioning with local hyperthermia to elevate intratumoral interstitial fluid flow,[4,5] delivery of transient anti-angiogenic therapies to temporarily increase blood flow,[6] and administration of anti-vascular endothelial growth factor receptor antibody to improve tissue perfusion[7]. While both morphologic and functional vasculature normalization have shown to temporarily improve agent perfusion to facilitate intratumoral delivery, remodeling processes occur that, ultimately, reduce vessel permeability and impair nanoparticle transport inside the tumor[8].

As only a fraction of an injected dose reaches the TME through the vasculature due to high interstitial fluid pressure,[9] supporting methodologies are needed to achieve tumor uptake and retention. Strategies to enhance particle accumulation into specific tumor regions include magnetic nanoparticles directed by external magnets,[10,11] ultrasound-mediated delivery to induce mechanical membrane stretching and pore formation,[12] tumor recruitment of nanoparticle-containing monocytes and macrophages,[13] and pH-responsive surface coatings which improve retention upon entering an acidic TME.[14,15] However, challenges related to scale-up and resource-efficiency limit their use.[16] These techniques also depend on additional external environmental or

internal factors, such as chemoattractive gradients needed to recruit nanoparticle-loaded monocytes or metabolic shifts to direct nanoparticle accumulation.

Regarding Gold Nanoparticles (GNPs), those ranging from 40-50 nm in diameter have been reported to accumulate predominantly (>80%) in the spleen and liver after systemic injection, with only a negligible fraction (~1%) localized inside the tumor. This reduced dose within the tumor, attributed to their sequestration by the reticuloendothelial system, results in suboptimal nanoparticle uptake and heterogeneous GNP spatial distribution that significantly diminishes therapeutic and diagnostic efficacy.[17,18] Loco-regional administration of nanotherapeutics mitigates many issues related to dose reduction following systemic exposure, overcoming important biological barriers to absorption in solid tumors such as stiffening of the extracellular matrix (ECM) and increased interstitial pressure.[19,20] Despite the limitations of intratumoral injection, such as the inability to directly target inaccessible metastatic lesions[21] and deep-seated tumors,[22] these challenges can be resolved through initiation of a host immune response and abscopal effect[23] to induce regression of distant untreated lesions.[24] Local, intratumoral delivery provides direct access to organized tertiary lymphoid structures within the tumor,[22] subsequently targeting lymphocytes and other immune cells that travel through lymphatic vessels. Understanding how loco-regional agents accumulate after intratumoral injection within the TME could advance our ability to molecular engineer them such that they distribute with higher concentrations at regions of enriched biomarkers or immune cells.

In addition to administration method, the intratumoral GNP distribution profile is strongly dependent upon their physicochemical properties; especially size, surface charge, surface functionalization, and shape.[25–28] We previously demonstrated the importance of surface passivation to control GNP distribution in a murine model of lung cancer.[29–31] However, a

thorough understanding of the effect of these properties to customize the design of GNPs to achieve the desired pharmacokinetics and spatiotemporal distribution profile inside tumors could be the holy grail of cancer nanomedicine, promising to advance drug delivery and optimize treatment outcome.

We demonstrate the ability to spatially control delivery of intratumorally injected GNP (zonal delivery) by leveraging different surface chemistries while minimizing variables in administration through injection with a syringe pump set at a constant dispense volume and flow rate. We experimentally observed differences in the intratumoral distribution patterns of GNPs coated with three different chemical moieties (citrate, PTE, and PEG). To mechanistically characterize these differences in GNP intratumoral distribution patterns, studies are complemented with mathematical modeling[32–34] of particle transport following intratumoral injection that considers particle reactivity over time.

Nanoparticle transport modeling has traditionally focused on tumoral delivery following systemic injection[32,34] rather than local. To this end, Mahesh et al. modeled nanoparticle tumoral transport following intratumoral injection using a convection-diffusion equation, and studied the effects of nanoparticle size, injection site, and vascular normalization on intratumoral distribution.[35] They incorporated interstitial fluid flow to obtain interstitial fluid pressure and velocity profiles in the tumor, allowing them to investigate transvascular clearance of the nanoparticles from the tumor interstitium. However, their model does not include nanoparticle interaction with the cellular components and ECM of the tumor. Similarly, Klapproth et al. developed a physiologically-based pharmacokinetic model to study whole-body distribution of superparamagnetic iron oxide nanoparticles following intratumoral injection and compared results to intravenous injection.[36] Their model is limited to the temporal evolution of nanoparticle

concentration inside the tumor and other organs and does not study nanoparticle spatial distribution profiles. Here, we hypothesized that upon intratumoral injection, nanoparticle transport in the tumor interstitium is strongly governed by nanoparticle interaction with cancerous cells and components of the ECM, which in turn is affected by differences in surface chemistries, leading to distinct intratumoral distribution patterns of the GNPs. To test our hypothesis, we modeled GNP transport following intratumoral injection using reaction-diffusion equations, which simulate the spatiotemporal evolution of GNPs inside the tumor. We chose a macroscopic scale continuum approach adapted from our previous work involving transport modeling of hydrogel-embedded nanoparticles injected intratumorally into glioblastoma tumors.[37] Integration of mathematical modeling with in vivo experimentation allows us to quantitatively characterize the nanoparticles biodistribution intratumorally towards the establishment of zonal-directed drug delivery within a tumor. These exciting results provide a foundation for the development of region-specific cargo delivery that can advance our ability to modulate various processes driving cancer progression as well as provide control over the retention and distribution of agents toward their specific surface target within the TME.

## RESULTS AND DISCUSSION

**In vitro uptake of GNPs is governed by their surface chemistry.** In this work, we synthesized spherical GNPs using the citrate reduction method[38] and surface functionalized them with either lipid bilayers (PTE) or polyether monolayers (PEG), two biocompatible coatings commonly used to mimic biological membranes[39,40] and improve nanoparticle stealth[41]. We selected GNPs because they can be visualized both in vitro using electron microscopy[42] and in

vivo using micro computed tomography[43] due to their superior x-ray absorption proprieties[44]. Schematic 1 shows GNPs natively stabilized with citrate or surface passivated with either PTE or PEG using conjugated thiol linkers. The synthesis and characterization of these native nanomaterials have been previously described in detail.[29,30,45] Surface chemistry modifications were achieved as described in the methods section. The resultant solutions appeared deep red in color and contained monodisperse spherical nanoparticles with hydrodynamic diameters of 39.77 ± 2.06 nm, 51.66 ± 0.58 nm, and 56.80 ± 0.55 nm for citrate-GNPs, PTE-GNPs, and PEG-GNPs, respectively (Figure S1A-C). All three surface passivations resulted in negatively charged particles (Figure S1D) with an observed 3-5 nm shift of their localized surface plasmon resonance due to passivation with either PTE or PEG (Figure S1E). All three nanoformulations also displayed concentration dependent x-ray attenuation with signal intensities stronger than that of a standard iodine-based contrast agent, Omnipaque350 (Figure S1F).

In order to determine if the modified surface chemistry of the GNPs affected particle uptake within cancer cells, we performed visualization studies using scanning transmission election microscopy along with elemental analysis to quantify differences in cellular gold content. Cancer cells from established murine (LLC) and human (HeLa) models were treated with each nanoformulation and cultured for 24 hours prior to processing (Figure S2). Citrate passivated particles were more greatly internalized within LLC cells as demonstrated by the large endocytic vesicles containing dark clusters, while particles passivated with PTE and PEG were found to a lesser degree (Figure 1A). Evidence of visualization correlated with elemental analysis where the intracellular gold content from citrate-GNPs was similar in both HeLa and

LLC cell lines and significantly (**$p < 0.005$) greater than that of the PTE-GNPs and PEG-GNPs (Figure 1B,D). Interestingly, PTE-GNPs were more toxic on HeLa cells than LLC cells when compared with their nascent particles (citrate) and PEGylated forms (Figure 1C,E). No dose-dependent cytotoxic effect was highlighted in any cell line.

**GNP diffusion patterns are dependent on surface chemistry.** Tumors were induced in mice through subcutaneous injection of LLC cells on their flank (see methods) and once the tumor volumes reached ~200 $mm^3$, baseline images from the tumor bearing animals were obtained with μCT. The animals were intratumorally administered either citrate, PTE, or PEG coated gold nanoparticles via syringe pump, and then imaged again with μCT immediately post-administration (Day 0) as well as on days 3, 6, and 9. Following controlled intratumoral injection, we observed via CT imaging that the citrate-GNPs consistently agglomerated as single clusters, a phenomenon also reported by our group after manual injection[30], while the PTE-GNPs and PEG-GNPs diffused predominantly in the tumor periphery. In vivo results demonstrated remarkable differences in the intratumoral diffusion of the GNPs depending on the surface passivation. The results are supported by gross inspection of the particles localized to different regions of the tumor (Figure 2A), quantification of the amount of intratumoral gold over time with inductively coupled plasma - optical emission spectrometry (ICP-OES) (Figure 2B) and tracking GNP localization within the solid tumor using μCT (Figure 2C). Interestingly, each surface functionalization presents a different pattern of intratumoral diffusion. In Figure 2D, x-ray attenuation of the nanoparticle treated tumors are reported over time and compared with the tumor baseline signal. Attenuation levels of the tumors after GNP injection

demonstrate significant changes between the PTE and PEG passivation 3- and 6-days post-injection (*$p = 0.01$, *$p = 0.03$). When comparing with the nascent particles, PTE-GNPs displayed x-ray attenuation similar in intensity, while PEG-GNP attenuation values were significantly lower 6- and 9-days post-injection (#$p = 0.03$, #$p = 0.04$). Despite this decrease, the PEG-GNPs still displayed an x-ray attenuation signal ~35% greater than the tumor background 9-days post-injection, demonstrating the capability of these particles to be tracked over time due to their high x-ray absorption properties. Experimental results from elemental analysis (Fig. 2B) and CT attenuation (Fig. 2D) significantly correlate using Pearson correlation analysis ($p = 0.004$). Accumulation of nascent and functionalized GNPs in other organs over time is shown in the Supporting Information (Figure S3). The highest concentration of GNPs was found in both the liver and spleen which offer a high number of extravasation sites. However, less than 10% of the ID was found in these organs without any significant differences between both treatment groups and days. This result confirms the advantages of loco-regional administration in preventing unwanted accumulation of our nanotherapeutic in non-specific sites.

**Intratumoral transport modeling of GNPs**. Experimental results highlighting the different GNP zonal distributions dependent on particle surface passivation were confirmed through a parsimonious mathematical model of GNP transport following intratumoral injection, adapted from our previous work.[37] Since citrate coated GNPs have the smallest diameter (Figure S1), this nanoformulation can be expected to have the highest diffusivity (as per Stokes-Einstein equation) and thus, the highest intratumoral coverage area. However, as observed in Figure 2A,C, the intratumoral coverage area of the citrate coated GNPs was the lowest, which led us to hypothesize that surface functionalization-induced interaction of NPs with the tumor

microenvironment competes with the effects of size-dependent diffusion on NP transport. Thus, the mathematical model was based on reaction-diffusion equations to investigate the relative effect of NP diffusivity and reactivity on the spatiotemporal evolution of GNPs inside the tumor. To characterize the relative strength of reactivity and diffusivity of GNPs, we defined a dimensionless parameter referred to as the Damköhler number ($D_a$) and tuned it to reproduce the experimental observations qualitatively.

To complement the experimental in vivo timeline (Fig. 2A,C), snapshots of the tumor mathematical model simulations are presented at days 3, 6, and 9 post-injection (Figure 2E). The area coverage of NPs in the tumor domain is indirectly proportional to their Damköhler number ($D_a$). This indirect relationship suggests that GNPs with a greater rate of reaction to the tumor microenvironment tend to travel the least distance from the site of injection. The simulation results are in good qualitative agreement with the experimental observations for the GNPs, indicating that citrate coated GNPs remain more localized near the site of injection due to their high reactivity ($D_a = 0.1$), unlike the less reactive PTE- ($D_a = 0.01$) and PEG-coated GNPs ($D_a = 10^{-5}$) which distribute more widely across the tumor interstitium, with PEGylated GNPs showing the greatest coverage area. We further confirm this interpretation by quantifying the concentration kinetics of bound and free (unbound) GNPs in the simulations. As shown in Figure 2F**,** the concentration of bound GNPs (red curves) around the site of injection (off-centered and set at a distance $\frac{R_{\mathrm{tum}}}{2}$ from the center of the tumor on its equator) follows the order $D_a = 0.1 > D_a = 0.01 > D_a = 1e-5$, while the reverse is the case for free NP concentration (blue curves). The average concentration of unbound GNPs across the

tumor diameter tends to decrease over time, with the highest change observed for the highly reactive citrate-GNPs. This indicates that less reactive GNPs can stay as freely diffusing for a longer period, thereby allowing such particles to diffuse farther away from the site of injection in a larger quantity, eventually leading to a more homogeneous particle distribution across the tumor diameter. It can thus be inferred from these numerical experiments that more reactive GNPs tend to distribute less across the tumor interstitium compared to less reactive GNPs, which tend to diffuse more.

**GNPs accumulate in different intratumoral zones depending on their surface chemistry.** To better quantify GNP zonal accumulation intratumorally, we performed local elemental analysis, sectioning and digesting each section of each tumor separately. As shown in Figure 3, we chose to cut the tumors in 4 regions and quantify the gold (n = 4 tumors) 3 and 6 days post-injection. Interestingly, the data not only confirms differences between groups treated with functionalized and nascent particles but also demonstrates that PTE- and PEG-GNPs accumulate to a greater degree in the lateral periphery over 3 days when compared with the citrate-GNPs.

**The histopathological profile of GNP intratumoral diffusion is dependent on particle surface chemistry.** The consistently observed zonal distribution pattern delineated between nanoformulation groups was also highlighted by histopathology (Figure 4). Solid tumor nodules were identified in the mice both visually and with μCT (Figure 4A-D), harvested and photographed (Figure 4E-H) and stained with hematoxylin and eosin (H&E) (Figure 4I-L). For comparison across the different treatment groups, we show a representative 2D central slice at

20x magnification which revealed dense tumor growth within the fibroadipose tissue. The tumors consist of numerous irregular nuclei with frequent mitotic figures. In the untreated group, the tumors were highly viable and mitotically active with only rare small foci of apoptosis. The treatment groups showed a border zone (Figure 4J-K white arrow) with distinct areas of viable tumor bordering areas of tumor necrosis (smaller foci). Interestingly, the patterns of necrosis in the treated animals were similar to the GNP diffusion patterns. The citrate-GNPs were primarily aggregated in the tumor center along with observed necrosis, the PTE-GNPs consisted of multiple clusters throughout similar to the necrosis pattern, and the PEG-GNPs concentrated at the tumor periphery where necrosis was found along with extension of the particles into the surrounding soft tissues. Surprisingly, while all the nanoformulations originate from the same material, only the PEG-GNPs traveled across the tumor boundary and into the surrounding stromal cells, demonstrating access to a secondary target region. While most researchers focus on outside-in drug delivery and overcoming the stromal boundary to penetrate into the tumor, these results show an inside-out directed delivery into the surrounding stromal cells, which supports and maintains the integrity of the tumor mass, thereby making it an important region to target.

## CONCLUSION

We investigated GNP interactions with the tumor microenvironment for nascent particles as well as particles surface passivated with lipid bilayers (PTE) and polyether monolayers

(PEG). We discovered in vivo different zone-specific patterns of particle accumulation in the tumor dependent on surface functionalization using a murine model of lung cancer. Ultimately, we predicted the spatiotemporal evolution of GNPs by modeling their intratumoral transport with reaction-diffusion equations. Using our parsimonious modeling approach, we demonstrated the mechanistic basis for the effect of surface functionalization on intratumoral GNP transport that has implications for drug delivery and treatment outcome. While the model assumed simplifications such as a non-growing tumor and the absence of advection, these assumptions do not necessarily impact the qualitative nature of our results. Importantly, we demonstrate that the characterization of GNPs using the Damköhler number ($D_a$) can be a valuable means to understand the impact of GNP properties on their transport behavior. While $D_a$ values were arbitrarily chosen as a proof of concept in the current study, future in vitro experiments can provide the necessary values of reaction rates to calculate $D_a$ and prospectively predict the expected intratumoral behavior of GNPs.

For the field of cancer nanomedicine, there are several fundamental and applied research directions that can be considered. From an applied perspective, a mathematical framework that allows for particle distribution predictions based on surface properties could revolutionize the current methods of personalized medicine. Several applications have been identified in the last decade for gold nanoparticles in cancer treatment. They can be used as cargo for chemotherapeutics, mediators for photothermal therapy, and as contrast agents for imaging, helping to track tumor size and determine molecular signatures. However, these applications have been limited by the poor and heterogeneous accumulation of GNPs within tumor tissues.

For this reason, mathematical simulations and in silico approaches may help optimize a combination of surface properties to better intratumorally deliver a nanotherapeutic to a targeted region of the tumor.

In this work, we used reaction-diffusion equations to model the intratumoral transport of nanoparticles and observed that the transport behavior of particles with high reactivity (greater Damköhler number) resulted in greater distribution across the tumor, while those with low reactivity remained localized. Using a reproducible intratumoral delivery approach (constant injection rate), we experimentally observed that changes in particle surface passivation affected transport behavior and resulted in remarkably different distribution patterns within the TME as assessed through different modalities (imaging, elemental analysis, and histology). Overall, the PEG functionalized GNPs consistently diffused in the tumor periphery and resulted in the greatest tumoral surface coverage, permeating beyond the cancer cells and into the stroma. As the stroma is known to play a role in promoting tumor development and metastasis, permeation into this region allows for access across the tumor-stroma barrier for therapeutic targeting. Finally, since the stroma (typically not targeted by standard anticancer therapies) can induce therapeutic resistance, its role in disease progression should not be overlooked, and identifying methods to target and deliver drugs into this region as well as other zones within the TME would offer a more comprehensive and integrative treatment approach.

## METHODS

**Animal Model**. All experiments conducted on the animals were approved for study (protocol # IS00005178 approved 6 May 2019 and protocol # IS00005819 approved 26 March 2021) by the Institutional Animal Care and Use Committee (IACUC) at the Houston Methodist Research Institute and were performed according to the principles of the NIH Guide for the Care and Use of Laboratory Animals, the provisions of the Animal Welfare Act, PHS Animal Welfare Policy, and the policies of the Houston Methodist Research Institute. Housing and care were provided in accordance with the regulations of the Animal Welfare Act and recommendations of the Guide for the Care and Use of Laboratory Animals. Six-week-old female C57BL/6 mice (Taconic Biosciences) (n=60) were used in this study. Two million Lewis Lung Carcinoma (LLC) cells were suspended in 100 μL of PBS (Cytiva) and injected subcutaneously into the right flank of the mice with an average weight of 18.28 ± 1.68 g. Tumors were grown for 8 days to ~200 $mm^3$ before GNP treatment (Figure S4).

**Chemicals and Reagents.** All chemicals were used without further purification. Deionized water was provided by a Millipore Milli-Q Integral 10 Water Purification System (Millipore Sigma).

*ICP-OES Chemicals.* Acids ($HNO_3$, HCl) were purchased as trace metal grade (ThermoFisher Scientific). The gold pure standard solution (Au 1000 μg/mL in 10% HCl and 1% $HNO_3$) was purchased from Perkin Elmer. Yttrium (1000 mg/L) was used as internal standard and purchased from Sigma-Aldrich. Seven standards were prepared to generate a calibration curve for Au content (100 μg [Au]/L, 250 μg [Au]/L, 500 μg [Au]/L, 1000 μg [Au]/L, 2500 μg [Au]/L, 5000 μg [Au]/L, and 10000 μg [Au]/L), as dilutions from the gold pure standard solution. All

measurements were performed on triplicate samples (or more when indicated) using a Varian 720-es ICP spectrometer (Agilent). All elemental analyses were performed using the ICP Expert II software (Agilent) by averaging the signal from the 242.794 nm and 267.594 nm emission lines. Each of the samples were filtered using 0.22 μm filters (MilliporeSigma) prior to ICP-OES measurement.

**Nanoparticle Synthesis and Characterization.** Gold nanoparticles were prepared as previously described[29,30]. Briefly, gold nanoparticles (~35 nm in diameter) were synthesized by boiling 4.8 mL of 0.039 M aqueous citrate (Sigma-Aldrich) and 7 mL of 0.033 M gold (III) chloride (Sigma-Aldrich) in 600 mL of deionized water until a transition in color from yellow to black occurred, and the colloidal solution appeared dark red. After GNP synthesis, the pH of the solution was measured to be 3.6. 1 M NaOH solution (Fisher Scientific) was added dropwise to the solution to adjust the pH to 6.0. GNPs were centrifuged at 1500*g* for 5 min in Amicon Ultra-15 100K filters (Sigma-Aldrich). Nanoparticle concentration was measured by ICP-OES and ultraviolet visible (UV–vis) spectroscopy and nanoparticle size was determined by dynamic light scattering (DLS) and scanning transmission electron microscopy (sTEM).

**Surface functionalization of concentrated GNPs with PTE.** Concentrated GNPs were conjugated to phosphothioethanol (PTE) using thiol chemistry. 1,2-dihexadecanoyl-sn-glycero-3-phosphothioethanol (sodium salt) (730 Da, 16:0 PTE; Avanti Polar Lipids) was dissolved in 200 proof ethanol (ThermoFisher). The PTE solution (1.45 mg/mL, 118 μL) was added to the GNP solution (18.56 mg/mL, 500 μL) at a ratio of 1 PTE molecule/nm$^2$ and incubated for 1 h at room temperature to let the ethanol evaporate completely. Once

completely evaporated, the ethanol was replaced with the same volume of deionized water (118 μL).

**Surface functionalization of concentrated GNPs with PEG.** Concentrated GNPs were conjugated to polyethylene glycol (PEG) using thiol chemistry. Poly(ethylene glycol) methyl ether thiol (6000 Da, mPEG-SH; Sigma-Aldrich) was dissolved in deionized water at a concentration of 1.2 mg/mL. The mPEG-SH solution (1.2 mg/mL, 118 μL) was added to the GNP solution (18.56 mg/mL, 500 μL) at a ratio of 1 PEG molecule/nm$^2$ and incubated for 1 h at room temperature.

**In Vitro Cytotoxicity and GNP Uptake.** LLC and HeLa cells were obtained from the American Type Culture Collection (ATCC). Cell subculturing and GNP-based treatment and procedures have been previously described[29,30]. For each cell line, we investigated three groups of GNP treatment (citrate-GNPs, PTE-GNPs, and PEG-GNPs) with two different treatment doses (15 μg [Au]/mL per well and 50 μg [Au]/mL per well). The amount of GNPs internalized by each of these cell lines as well as cell viability after particle treatment were measured in triplicate wells.

*MTT Assay for cytotoxicity.* Briefly, cells were seeded ($4 \times 10^4$ cells/well) into 96-well plates (Thermo Fisher Scientific) and allowed to attach overnight. Cells were treated with each of the nanoformulations and incubated for 24 h. 10 μL of MTT Reagent (ATCC) was added to each well and the plate incubated for 2 h or until a purple precipitate appeared. Then, 100 μL of Detergent Reagent for MTT (ATCC) was added to each well to solubilize the purple

precipitate for 4 h prior to absorbance measurements at 570 nm and 690 nm using a Synergy™ H4 Hybrid Microplate Reader (BioTek Instruments, Inc.).

*ICP-OES quantification of GNP uptake.* Briefly, cells were seeded ($3 \times 10^5$ cells/well) into 6-well plates (Thermo Fisher Scientific) and allowed to attach overnight. Cells were treated with each of the nanoformulations and incubated for 24 h. Cells were washed with sterile 1x PBS (Cytiva), detached with 0.25% trypsin-0.53 mM EDTA solution (Thermo Fisher Scientific), neutralized with complete media, counted with an automated cell counter (Invitrogen) using a solution of 0.4% Trypan Blue (Thermo Fisher Scientific), and pelleted. All collected pellets were digested for 1 h in a 1 mL solution of aqua-regia (1:3 $HNO_3$ to HCl) and then diluted in 2 mL of acidic solution (10% HCl, 1% $HNO_3$) for ICP-OES.

*sTEM assessments of GNP intracellular internalization.* Sample preparation and procedures for electron microscopy were previously reported[46]. Images were obtained using the bright field setting in sTEM mode (FEI Nova NanoSEM 230) under a vacuum of 15 kV.

**In Vivo GNP biodistribution.** Mice received intratumoral injections of citrate-GNPs, PTE-GNPs, or PEG-GNPs (50 μL, 15 mg [Au]/mL, $n$ = 20 mice/group), once their tumor volumes reached ~200 $mm^3$. To minimize the possible errors due to the challenges of consistent intratumoral administration and to assure maximum reproducibility, all injections were performed with an automatic syringe pump (KD Scientific Inc., 0.43 μL/s) while the animals were maintained under anesthesia with isoflurane.

*In vivo imaging and intratumoral GNP tracking.* In vivo imaging was performed with micro-Computed Tomography (μCT) using a Siemens Inveon Multi-Modality System and an Inveon

Acquisition Workplace. Imaging parameters were the following: slice thickness, 103.25 μm; in-plane resolution, 103.25 μm; tube voltage, 80 kV; tube current, 500 μA; exposure time, 240 ms. Baseline images were acquired pre-injection and immediately after injection. Follow-up imaging occurred on days 3 ($n$ = 3 mice/group), 6 ($n$ = 3 mice/group), and 9 ($n$ = 3 mice/group) post-injection of each treatment. Imaging analysis was performed with 3D Slicer (v4.11) on this dataset of acquired images.

*Intratumoral GNP content and biodistribution.* Biodistribution of the GNPs was determined after intratumoral injection in a mouse model of lung cancer by quantifying the amount of gold in the solid tumor as well as in different organs (liver, spleen, lung, heart, kidneys, brain) and blood using ICP-OES. Mice sacrifice and tissue collection occurred 3 ($n$ = 8 mice/group), 6 ($n$ = 8 mice/group), and 9 ($n$ = 4 mice/group) days post-injection. Blood was collected via cardiac puncture immediately after death and tissues were weighed, flash frozen in liquid nitrogen, and stored at –80 °C for further analysis. For elemental analysis, the whole tissue was digested, except certain tumors on day 3 ($n$ = 4 mice/group) and day 6 ($n$ = 4 mice/group) that were further sub-sectioned. From each of these tumors, 4 dissections were obtained (medial periphery, medial core, lateral periphery, and lateral core), following the previously described approach[31]. Samples were digested as previously described[30]. Briefly, each tissue or blood sample was kept for 1 h in 2 mL of fresh aqua regia at 60 °C until complete digestion, and then diluted in 8 mL of acidic solution (10% HCl, 1% $HNO_3$). The gold content of each sample was measured and normalized to the injected dose (ID) of the GNPs and expressed as percentage of the ID.

*Histopathology*. At day 9 post-injection, harvested tumors were fixed in 10% formalin, paraffin embedded, and sectioned. Each section was stained with hematoxylin and eosin (H&E) to evaluate the effects of nanoparticle treatment type on intratumoral zonal distribution. All samples were examined using a bright field microscope (EVOS Cell Imaging System Models, Thermo Fisher Scientific).

**Model development.** Following intratumoral injection, GNPs in the tumor interstitium diffuse away from the site of injection, while interacting with the ECM and cancer cells. Thus, a fraction of the injected mass of GNPs continues to bind with cancer cells and components of the ECM, while the remaining unbound fraction continues to diffuse away. We describe the spatiotemporal dynamics of the free and bound GNPs with the following partial differential equations (PDEs).

*Equation for concentration of free GNPs* ($\boldsymbol{C_{NP}^{f}(\underline{x}, t)}$):

$$\frac{\partial C_{\mathrm{NP}}^{f}(\underline{x},t)}{\partial t} = \overbrace{D_{\mathrm{NP}} \cdot \nabla^2 C_{\mathrm{NP}}^{f}(\underline{x}, t)}^{\text{Diffusion}} - \overbrace{I(\underline{x}, t)}^{\text{Interaction}} \quad (1)$$

where $D_{\mathrm{NP}}$ represents the diffusivity of NPs in tumor interstitium and $I(\underline{x}, t)$ is the NP interaction term that describes the collective rate of interaction of GNPs with cancer cells and components of the ECM and is characterized as a Michaelis-Menten process, such that $I(\underline{x}, t) = I_{\max} \cdot \frac{C_{\mathrm{NP}}^{f}(\underline{x},t)}{K_m + C_{\mathrm{NP}}^{f}(\underline{x},t)}$. Here, $I_{\max}$ is the maximal rate of reaction and $K_m$ is the Michaelis-Menten constant. Note that in our parsimonious model we have ignored advection as a

transport mechanism of GNPs due to the occurrence of high interstitial fluid pressure in solid tumors[47].

*Equation for concentration of bound GNPs* ($\boldsymbol{C_{NP}^{b}(\underline{x}, t)}$):

$$\frac{\partial C_{\mathrm{NP}}^{b}(\underline{x},t)}{\partial t} = \overbrace{I(\underline{x}, t)}^{\text{Interaction}} \quad (\mathbf{2})$$

We assume that GNPs once bound cannot unbind, hence the equation for bound NPs only contains the previously defined interaction term.

*Numerical solution.* To solve the above PDEs, we used a numerical approach known as the finite difference method, for which we assumed a two-dimensional square lattice grid discretized into square elements to calculate the diffusion and interaction of GNPs at discrete time points (Figure S5). The 2D domain has a side $l = 2$ cm and is discretized into 400x400 elements, with each element of side $\Delta = 50$ μm. The tumor is assumed to be a 2D circle located at the center of the domain and has a radius $R_{\mathrm{tum}} = 0.5$ cm. For simplicity, we assume the tumor to be static, i.e., it does not evolve over time. At every time step, the concentration of free and bound GNPs at a given grid element $(i, j)$ is estimated by the following expressions based on the explicit method:

$$C_{i,j}^{f,\mathrm{t+dt}} = C_{i,j}^{f,\mathrm{t}} + \left( D_{\mathrm{NP}} \frac{\left( C_{i+1,j}^{f,\mathrm{t}} + C_{i-1,j}^{f,\mathrm{t}} + C_{i,j+1}^{f,\mathrm{t}} + C_{i,j-1}^{f,\mathrm{t}} - 4C_{i,j}^{f,\mathrm{t}} \right)}{\Delta^2} - I_{\max} \frac{C_{i,j}^{f,\mathrm{t}}}{K_m + C_{i,j}^{f,\mathrm{t}}} \right) dt \quad (\mathbf{3})$$

$$C_{i,j}^{b,\mathrm{t+dt}} = C_{i,j}^{b,\mathrm{t}} + I_{\max} \frac{C_{i,j}^{f,\mathrm{t}}}{K_m + C_{i,j}^{f,\mathrm{t}}} \cdot dt \quad (\mathbf{4})$$

where subscripts $i$ and $j$ represent row and column number of a given grid element, respectively, and superscripts $f$ and $b$ indicate free and bound GNPs, respectively. We imposed a Neumann boundary condition at the tumor periphery such that $\frac{\partial C}{\partial x} = 0$, i.e. no flux occurs at the tumor boundary. For the initial conditions, we assumed a concentration of free GNPs $C_0$ at the site of injection (at a distance $\frac{R_{\mathrm{tum}}}{2}$ from the center of the tumor on its equator), and zero concentration everywhere else. All the simulations were performed in MATLAB R2020b.

*Model parameter estimation.* The various model parameters are defined in Table S1. One of the key model parameters that we discuss here is referred to as the Damköhler number ($D_a$), which is a dimensionless number defined as the ratio of rate of reaction to the rate of diffusion of GNPs, such that $D_a = \frac{I_{\max}}{D_{\mathrm{NP}}/R_{\mathrm{tum}}^2}$. It is worth noting that $D_a$ is implicitly divided by a unit concentration to make $D_a$ dimensionless. Since the gold core of the various GNPs investigated in this study have a comparable size ($\phi_{\mathrm{NP}}$~30 nm), we assumed the same rate of particle diffusion among groups (given that rate of diffusion is a function of particle size as per the Stokes-Einstein equation). However, we hypothesized that due to the difference in surface chemistry of GNPs, the rate of reaction across groups will vary. Hence, to simulate GNPs with different rates of reaction (or $I_{\max}$), we use different $D_a$ numbers. Specifically, we model three different scenarios to compare the simulations to the three types of GNPs investigated in this study, such that $D_a = 0.1$

for highly reactive GNPs, $D_a = 0.01$ for moderately reactive GNPs, and $D_a = 10^{-5}$ for weakly reactive GNPs.

**Data and Statistical Analysis.** Experimental results are presented as a mean of three replicates (n = 3) ± standard error of the mean (s.e.m). Data were evaluated using a nonparametric two-way analysis of variance (ANOVA). Subsequent analysis occurred in terms of a Tukey's multiple comparison posthoc test (GraphPad Prism 9 software, USA). Data was considered significant when $^{*}p < 0.05$, $^{**}p < 0.01$, $^{***}p < 0.001$, and $^{****}p < 0.0001$.

ASSOCIATED CONTENT

*Conflict of Interest*: The authors declare no competing financial interest.

**Supporting Information**. Physiochemical properties and characterization of gold nanoparticles (photograph, sTEM image, hydrodynamic diameter and polydispersity index measured with dynamic light scattering, diameter measured from sTEM, zeta-potential measurements, absorption spectra, and x-ray absorption signal strength); optical microscope images of HeLa and LLC cells after 24 h of treatment; biodistribution of GNPs in organs calculated using ICP-OES; in vivo mice weight and tumor volumes; schematic of 2D modeling domain; table of model parameters for the mathematical simulations;. This material is available free of charge via the Internet at http://pubs.acs.org.

AUTHOR INFORMATION

**Corresponding Author**

Carly S. Filgueira - Department of Nanomedicine, Department of Cardiovascular Surgery, Houston Methodist Research Institute, 6670 Bertner Ave., R8-118, Houston, TX 77030, USA, orcid.org/0000-0002-3246-303X, e-mail: csfilgueira@houstonmethodist.org

**Authors**

Rossana Terracciano - Department of Nanomedicine, Houston Methodist Research Institute, 6670 Bertner Ave., R8-330.12, Houston, TX 77030, USA, orcid.org/0000-0001-5026-0589, e-mail: rterracciano@houstonmethodist.org

Yareli Carcamo-Bahena - Department of Nanomedicine, Houston Methodist Research Institute, 6670 Bertner Ave., R8-330.12, Houston, TX 77030, USA, e-mail: ycarcamo@houstonmethodist.org

Amber Lee R. Royal - Department of Nanomedicine, Houston Methodist Research Institute, 6670 Bertner Ave., R8-330.12, Houston, TX 77030, USA, e-mail: alrroyal@houstonmethodist.org

Luca Messina - Univestià degli Studi di Napoli Federico II, Naples, Italy, e-mail: lucamessinalm95@gmail.com

Jack Delk - Texas A&M University, College Station, TX, USA, e-mail: 20delkj@gmail.com

E. Brian Butler - Department of Radiation Oncology, Houston Methodist Research Institute, Houston, TX 77030, USA, e-mail: EButler@houstonmethodist.org

Danilo Demarchi - Department of Electronics and Telecommunications, Politecnico di Torino, Corso Castelfidardo, 39, 10129 Torino, Italy, orcid.org/0000-0001-5374-1679, e-mail: danilo.demarchi@polito.it

Alessandro Grattoni - Department of Nanomedicine, Department of Radiation Oncology, Department of Surgery, Houston Methodist Research Institute, 6670 Bertner Ave., Houston, TX 77030, USA, orcid.org/0000-0001-7888-422X, e-mail: agrattoni@houstonmethodist.org

Zhihui Wang - Mathematics in Medicine Program, Houston Methodist Research Institute, Houston, TX 77030 USA, orcid.org/0000-0001-6262-700X, e-mail: zwang@houstonmethodist.org

Vittorio Cristini - Mathematics in Medicine Program, Houston Methodist Research Institute, Houston, TX 77030 USA, Department of Imaging Physics, University of Texas MD Anderson Cancer Center, Houston, TX 77030, USA, Physiology, Biophysics, and Systems Biology Program, Graduate School of Medical Sciences, Weill Cornell Medicine, New York, NY 10022, USA, orcid.org/0000-0002-7909-4278, e-mail: vcristini@houstonmethodist.org

Prashant Dogra - Mathematics in Medicine Program, Houston Methodist Research Institute, Houston, TX 77030, USA, Department of Physiology and Biophysics, Weill Cornell Medical College, New York, NY 10022, USA, orcid.org/0000-0001-6722-7371, e-mail: pdogra@houstonmethodist.org

**Author Contributions**

R.T. and C.S.F. conceived the idea and designed the research. P.D. conceived the modeling study. R.T., Y.C. and A.L.R.R. conducted the experiments, including the synthesis of all nanomaterials, material characterizations, cell passaging and maintenance, cellular toxicity evaluation, in vitro measurements, mouse experiments, in vivo imaging and ICP analysis. P.D. and L.M. developed the model. J.D. and L.M. performed the modeling and simulation analysis. P.D., Z.W., and V.C. interpreted the modeling results. R.T. and C.S.F. analyzed all the experimental data. All authors contributed to editing and revising the manuscript. All authors have given approval to the final version of the manuscript.

ACKNOWLEDGMENT

This study was supported by the Golfers Against Cancer (A.G., E.B.B. and C.S.F.), funds from Houston Methodist Research Institute (C.S.F.), and the Cockrell Foundation (V.C., P.D.). The mathematical modeling work has been supported in part by the National Institutes of Health (NIH) Grants 1R01CA253865 (Z.W., V.C.), 1R01CA226537 (Z.W., V.C.), and 1R01CA222007 (Z.W., V.C.). The authors are grateful to the Houston Methodist Research Institute Electron Microscopy Core, the Houston Methodist Research Institute Translational Imaging PreClinical Imaging (Small Animal) Core, and the Houston Methodist Research Institute Research Pathology Core for their assistance with the electron microscope, in vivo imaging experiments, and histological sample preparation and evaluations, respectively. The funders had no role in study design, data collection and analysis, decision to publish, or preparation of the manuscript.

ABBREVIATIONS

GNPs, gold nanoparticles; ECM, extracellular matrix; ICP-OES, inductively coupled plasma - optical emission spectrometry; UV–vis, ultraviolet visible; DLS, dynamic light scattering; sTEM, scanning transmission electron microscopy.

REFERENCES

Commented [TR4]: Max 45. Avoid unnecessary citations


(1) Viswanath, D. I.; Liu, H.-C.; Huston, D. P.; Chua, C. Y. X.; Grattoni, A. Emerging Biomaterial-Based Strategies for Personalized Therapeutic in Situ Cancer Vaccines. *Biomaterials* **2022**, *280*, 121297. https://doi.org/10.1016/j.biomaterials.2021.121297.

(2) Liu, H.-C.; Viswanath, D. I.; Pesaresi, F.; Xu, Y.; Zhang, L.; Trani, N. D.; Paez-Mayorga, J.; Hernandez, N.; Wang, Y.; Erm, D. R.; Ho, J.; Susnjar, A.; Liu, X.; Demaria, S.; Chen, S.-H.; Teh, B. S.; Butler, E. B.; Chua, C. Y. X.; Grattoni, A. Potentiating Antitumor Efficacy Through Radiation and Sustained Intratumoral Delivery of Anti-CD40 and Anti-PDL1. *Int. J. Radiat. Oncol. Biol. Phys.* **2021**, *110* (2), 492–506. https://doi.org/10.1016/j.ijrobp.2020.07.2326.

(3) Chua, C. Y. X.; Jain, P.; Susnjar, A.; Rhudy, J.; Folci, M.; Ballerini, A.; Gilbert, A.; Singh, S.; Bruno, G.; Filgueira, C. S.; Yee, C.; Butler, E. B.; Grattoni, A. Nanofluidic Drug-Eluting Seed for Sustained Intratumoral Immunotherapy in Triple Negative Breast Cancer. *J Control Release* **2018**, *285*, 23–34. https://doi.org/10.1016/j.jconrel.2018.06.035.

(4) Li, L.; ten Hagen, T. L. M.; Bolkestein, M.; Gasselhuber, A.; Yatvin, J.; van Rhoon, G. C.; Eggermont, A. M. M.; Haemmerich, D.; Koning, G. A. Improved Intratumoral Nanoparticle Extravasation and Penetration by Mild Hyperthermia. *J. Control. Release* **2013**, *167* (2), 130–137. https://doi.org/10.1016/j.jconrel.2013.01.026.

(5) Mathuria, N.; Royal, A. L. R.; Enterría-Rosales, J.; Carcamo-Bahena, Y.; Terracciano, R.; Dave, A.; Valderrabano, M.; Filgueira, C. S. Near-Infrared Sensitive Nanoparticle-Mediated Photothermal Ablation of Ventricular Myocardium. *Heart Rhythm* **2022**, S1547-5271(22)01962-2. https://doi.org/10.1016/j.hrthm.2022.05.006.

(6) Li, W.; Zhao, X.; Du, B.; Li, X.; Liu, S.; Yang, X.-Y.; Ding, H.; Yang, W.; Pan, F.; Wu, X.; Qin, L.; Pan, Y. Gold Nanoparticle–Mediated Targeted Delivery of Recombinant Human Endostatin Normalizes Tumour Vasculature and Improves Cancer Therapy. *Sci. Rep.* **2016**, *6* (1), 30619. https://doi.org/10.1038/srep30619.

(7) Chen, Y.; Liu, X.; Yuan, H.; Yang, Z.; von Roemeling, C. A.; Qie, Y.; Zhao, H.; Wang, Y.; Jiang, W.; Kim, B. Y. S. Therapeutic Remodeling of the Tumor Microenvironment Enhances Nanoparticle Delivery. *Adv. Sci.* **2019**, *6* (5), 1802070. https://doi.org/10.1002/advs.201802070.

(8) Jiang, W.; Huang, Y.; An, Y.; Kim, B. Y. S. Remodeling Tumor Vasculature to Enhance Delivery of Intermediate-Sized Nanoparticles. *ACS Nano* **2015**, *9* (9), 8689–8696. https://doi.org/10.1021/acsnano.5b02028.

(9) Lammers, T.; Kiessling, F.; Hennink, W. E.; Storm, G. Drug Targeting to Tumors: Principles, Pitfalls and (Pre-) Clinical Progress. *J. Control. Release* **2012**, *161* (2), 175–187. https://doi.org/10.1016/j.jconrel.2011.09.063.

(10) Wagstaff, A. J.; Brown, S. D.; Holden, M. R.; Craig, G. E.; Plumb, J. A.; Brown, R. E.; Schreiter, N.; Chrzanowski, W.; Wheate, N. J. Cisplatin Drug Delivery Using Gold-Coated Iron Oxide Nanoparticles for Enhanced Tumour Targeting with External Magnetic Fields. *Inorganica Chim. Acta* **2012**, *393*, 328–333. https://doi.org/10.1016/j.ica.2012.05.012.

(11) Levin, C. S.; Hofmann, C.; Ali, T. A.; Kelly, A. T.; Morosan, E.; Nordlander, P.; Whitmire, K. H.; Halas, N. J. Magnetic–Plasmonic Core–Shell Nanoparticles. *ACS Nano* **2009**, *3* (6), 1379–1388. https://doi.org/10.1021/nn900118a.

(12) Snipstad, S.; Berg, S.; Mørch, Ý.; Bjørkøy, A.; Sulheim, E.; Hansen, R.; Grimstad, I.; van Wamel, A.; Maaland, A. F.; Torp, S. H.; Davies, C. de L. Ultrasound Improves the Delivery and Therapeutic Effect of Nanoparticle-Stabilized Microbubbles in Breast Cancer Xenografts. *Ultrasound. Med. Biol.* **2017**, *43* (11), 2651–2669. https://doi.org/10.1016/j.ultrasmedbio.2017.06.029.

(13) Choi, M.-R.; Stanton-Maxey, K. J.; Stanley, J. K.; Levin, C. S.; Bardhan, R.; Akin, D.; Badve, S.; Sturgis, J.; Robinson, J. P.; Bashir, R.; Halas, N. J.; Clare, S. E. A Cellular Trojan Horse for Delivery of Therapeutic Nanoparticles into Tumors. *Nano Lett* **2007**, *7* (12), 3759–3765. https://doi.org/10.1021/nl072209h.

(14) Crayton, S. H.; Tsourkas, A. PH-Titratable Superparamagnetic Iron Oxide for Improved Nanoparticle Accumulation in Acidic Tumor Microenvironments. *ACS Nano* **2011**, *5* (12), 9592–9601. https://doi.org/10.1021/nn202863x.

(15) Bishnoi, S. W.; Rozell, C. J.; Levin, C. S.; Gheith, M. K.; Johnson, B. R.; Johnson, D. H.; Halas, N. J. All-Optical Nanoscale PH Meter. *Nano Lett.* **2006**, *6* (8), 1687–1692. https://doi.org/10.1021/nl060865w.

(16) Liu, J. F.; Jang, B.; Issadore, D.; Tsourkas, A. Use of Magnetic Fields and Nanoparticles to Trigger Drug Release and Improve Tumor Targeting. *Wiley Interdiscip. Rev. Nanomed. Nanobiotechnol.* **2019**, *11* (6), e1571. https://doi.org/10.1002/wnan.1571.

(17) England, C. G.; Huang, J. S.; James, K. T.; Zhang, G.; Gobin, A. M.; Frieboes, H. B. Detection of Phosphatidylcholine-Coated Gold Nanoparticles in Orthotopic Pancreatic Adenocarcinoma Using Hyperspectral Imaging. *PLoS One* **2015**, *10* (6), e0129172. https://doi.org/10.1371/journal.pone.0129172.

(18) Huo, S.; Ma, H.; Huang, K.; Liu, J.; Wei, T.; Jin, S.; Zhang, J.; He, S.; Liang, X.-J. Superior Penetration and Retention Behavior of 50 Nm Gold Nanoparticles in Tumors. *Cancer Res.* **2013**, *73* (1), 319–330. https://doi.org/10.1158/0008-5472.CAN-12-2071.

(19) Garrastazu Pereira, G.; Lawson, A. J.; Buttini, F.; Sonvico, F. Loco-Regional Administration of Nanomedicines for the Treatment of Lung Cancer. *Drug Delivery* **2016**, *23* (8), 2881–2896. https://doi.org/10.3109/10717544.2015.1114047.

(20) Chua, C. Y. X.; Ho, J.; Demaria, S.; Ferrari, M.; Grattoni, A. Emerging Technologies for Local Cancer Treatment. *Adv. Ther.* **2020**, *3* (9), 2000027. https://doi.org/10.1002/adtp.202000027.

(21) Marabelle, A.; Andtbacka, R.; Harrington, K.; Melero, I.; Leidner, R.; de Baere, T.; Robert, C.; Ascierto, P. A.; Baurain, J.-F.; Imperiale, M.; Rahimian, S.; Tersago, D.; Klumper, E.; Hendriks, M.; Kumar, R.; Stern, M.; Öhrling, K.; Massacesi, C.; Tchakov, I.; Tse, A.; Douillard, J.-Y.; Tabernero, J.; Haanen, J.; Brody, J. Starting the Fight in the Tumor: Expert Recommendations for the Development of Human Intratumoral Immunotherapy (HIT-IT). *Ann. Oncol.* **2018**, *29* (11), 2163–2174. https://doi.org/10.1093/annonc/mdy423.

(22) Melero, I.; Castanon, E.; Alvarez, M.; Champiat, S.; Marabelle, A. Intratumoural Administration and Tumour Tissue Targeting of Cancer Immunotherapies. *Nat. Rev. Clin. Oncol.* **2021**, *18* (9), 558–576. https://doi.org/10.1038/s41571-021-00507-y.

(23) Yasuda, K.; Nirei, T.; Tsuno, N. H.; Nagawa, H.; Kitayama, J. Intratumoral Injection of Interleukin-2 Augments the Local and Abscopal Effects of Radiotherapy in Murine Rectal Cancer. *Cancer Sci.* **2011**, *102* (7), 1257–1263. https://doi.org/10.1111/j.1349-7006.2011.01940.x.

(24) Mukhopadhyay, A.; Wright, J.; Shirley, S.; Canton, D. A.; Burkart, C.; Connolly, R. J.; Campbell, J. S.; Pierce, R. H. Characterization of Abscopal Effects of Intratumoral Electroporation-Mediated IL-12 Gene Therapy. *Gene Ther.* **2019**, *26* (1), 1–15. https://doi.org/10.1038/s41434-018-0044-5.

(25) Dogra, P.; Adolphi, N. L.; Wang, Z.; Lin, Y.-S.; Butler, K. S.; Durfee, P. N.; Croissant, J. G.; Noureddine, A.; Coker, E. N.; Bearer, E. L.; Cristini, V.; Brinker, C. J. Establishing the Effects of Mesoporous Silica Nanoparticle Properties on in Vivo Disposition Using Imaging-Based Pharmacokinetics. *Nat. Commun.* **2018**, *9* (1), 4551. https://doi.org/10.1038/s41467-018-06730-z.

(26) Goel, S.; Ferreira, C. A.; Dogra, P.; Yu, B.; Kutyreff, C. J.; Siamof, C. M.; Engle, J. W.; Barnhart, T. E.; Cristini, V.; Wang, Z.; Cai, W. Size-Optimized Ultrasmall Porous Silica Nanoparticles Depict Vasculature-Based Differential Targeting in Triple Negative Breast Cancer. *Small* **2019**, *15* (46), 1903747. https://doi.org/10.1002/smll.201903747.

(27) Goel, S.; Zhang, G.; Dogra, P.; Nizzero, S.; Cristini, V.; Wang, Z.; Hu, Z.; Li, Z.; Liu, X.; Shen, H.; Ferrari, M. Sequential Deconstruction of Composite Drug Transport in Metastatic Breast Cancer. *Sci. Adv. 6* (26), eaba4498. https://doi.org/10.1126/sciadv.aba4498.

(28) Wilhelm, S.; Tavares, A. J.; Dai, Q.; Ohta, S.; Audet, J.; Dvorak, H. F.; Chan, W. C. W. Analysis of Nanoparticle Delivery to Tumours. *Nat. Rev. Mater.* **2016**, *1* (5), 1–12. https://doi.org/10.1038/natrevmats.2016.14.

(29) Terracciano, R.; Sprouse, M. L.; Wang, D.; Ricchetti, S.; Hirsch, M.; Ferrante, N.; Butler, E. B.; Demarchi, D.; Grattoni, A.; Filgueira, C. S. Intratumoral Gold Nanoparticle-Enhanced CT Imaging: An in Vivo Investigation of Biodistribution and Retention. In *2020 IEEE 20th International Conference on Nanotechnology (IEEE-NANO)*; 2020; pp 349–353. https://doi.org/10.1109/NANO47656.2020.9183611.

(30) Terracciano, R.; Zhang, A.; Butler, E. B.; Demarchi, D.; Hafner, J. H.; Grattoni, A.; Filgueira, C. S. Effects of Surface Protein Adsorption on the Distribution and Retention of Intratumorally Administered Gold Nanoparticles. *Pharmaceutics* **2021**, *13* (2), 216. https://doi.org/10.3390/pharmaceutics13020216.

(31) Terracciano, R.; Carcamo-Bahena, Y.; Butler, E. B.; Demarchi, D.; Grattoni, A.; Filgueira, C. S. Hyaluronate-Thiol Passivation Enhances Gold Nanoparticle Peritumoral Distribution When Administered Intratumorally in Lung Cancer. *Biomedicines* **2021**, *9* (11), 1561. https://doi.org/10.3390/biomedicines9111561.

(32) Dogra, P.; Butner, J. D.; Chuang, Y.; Caserta, S.; Goel, S.; Brinker, C. J.; Cristini, V.; Wang, Z. Mathematical Modeling in Cancer Nanomedicine: A Review. *Biomed. Microdevices* **2019**, *21* (2), 40. https://doi.org/10.1007/s10544-019-0380-2.

(33) Dogra, P.; Butner, J. D.; Nizzero, S.; Ruiz Ramírez, J.; Noureddine, A.; Peláez, M. J.; Elganainy, D.; Yang, Z.; Le, A.-D.; Goel, S.; Leong, H. S.; Koay, E. J.; Brinker, C. J.; Cristini, V.; Wang, Z. Image-Guided Mathematical Modeling for Pharmacological Evaluation of Nanomaterials and Monoclonal Antibodies. *Wiley Interdiscip. Rev. Nanomed. Nanobiotechnol. WIRES NANOMED NANOBI* **2020**, *12* (5), e1628. https://doi.org/10.1002/wnan.1628.

(34) Dogra, P.; Butner, J. D.; Ruiz Ramírez, J.; Chuang, Y.; Noureddine, A.; Brinker, C. J.; Cristini, V.; Wang, Z. A Mathematical Model to Predict Nanomedicine Pharmacokinetics and

Tumor Delivery. *Comput. Struct. Biotechnol. J.* **2020**, *18*, 518–531. https://doi.org/10.1016/j.csbj.2020.02.014.

(35) Mahesh, N.; Singh, N.; Talukdar, P. A Mathematical Model for Understanding Nanoparticle Biodistribution after Intratumoral Injection in Cancer Tumors. *J. Drug Deliv. Sci. Technol.* **2022**, *68*, 103048. https://doi.org/10.1016/j.jddst.2021.103048.

(36) Klapproth, A. P.; Shevtsov, M.; Stangl, S.; Li, W. B.; Multhoff, G. A New Pharmacokinetic Model Describing the Biodistribution of Intravenously and Intratumorally Administered Superparamagnetic Iron Oxide Nanoparticles (SPIONs) in a GL261 Xenograft Glioblastoma Model. *Int J Nanomedicine* **2020**, *15*, 4677–4689. https://doi.org/10.2147/IJN.S254745.

(37) Brachi, G.; Ruiz-Ramírez, J.; Dogra, P.; Wang, Z.; Cristini, V.; Ciardelli, G.; Rostomily, R. C.; Ferrari, M.; Mikheev, A. M.; Blanco, E.; Mattu, C. Intratumoral Injection of Hydrogel-Embedded Nanoparticles Enhances Retention in Glioblastoma. *Nanoscale* **2020**, *12* (46), 23838–23850. https://doi.org/10.1039/D0NR05053A.

(38) Turkevich, J.; Stevenson, P. C.; Hillier, J. A Study of the Nucleation and Growth Processes in the Synthesis of Colloidal Gold. *Discuss. Faraday Soc.* **1951**, *11* (0), 55–75. https://doi.org/10.1039/DF9511100055.

(39) Levin, C. S.; Kundu, J.; Janesko, B. G.; Scuseria, G. E.; Raphael, R. M.; Halas, N. J. Interactions of Ibuprofen with Hybrid Lipid Bilayers Probed by Complementary Surface-Enhanced Vibrational Spectroscopies. *J. Phys. Chem. B* **2008**, *112* (45), 14168–14175. https://doi.org/10.1021/jp804374e.

(40) Kundu, J.; Levin, C. S.; Halas, N. J. Real-Time Monitoring of Lipid Transfer between Vesicles and Hybrid Bilayers on Au Nanoshells Using Surface Enhanced Raman Scattering (SERS). *Nanoscale* **2009**, *1* (1), 114–117. https://doi.org/10.1039/B9NR00063A.

(41) Levin, C. S.; Bishnoi, S. W.; Grady, N. K.; Halas, N. J. Determining the Conformation of Thiolated Poly(Ethylene Glycol) on Au Nanoshells by Surface-Enhanced Raman Scattering Spectroscopic Assay. *Anal. Chem.* **2006**, *78* (10), 3277–3281. https://doi.org/10.1021/ac060041z.

(42) Goldstein, A.; Soroka, Y.; Frušić-Zlotkin, M.; Popov, I.; Kohen, R. High Resolution SEM Imaging of Gold Nanoparticles in Cells and Tissues. *J. Microsc.* **2014**, *256* (3), 237–247. https://doi.org/10.1111/jmi.12179.

(43) Dou, Y.; Guo, Y.; Li, X.; Li, X.; Wang, S.; Wang, L.; Lv, G.; Zhang, X.; Wang, H.; Gong, X.; Chang, J. Size-Tuning Ionization To Optimize Gold Nanoparticles for Simultaneous Enhanced CT Imaging and Radiotherapy. *ACS Nano* **2016**, *10* (2), 2536–2548. https://doi.org/10.1021/acsnano.5b07473.

(44) Kim, D.; Park, S.; Lee, J. H.; Jeong, Y. Y.; Jon, S. Antibiofouling Polymer-Coated Gold Nanoparticles as a Contrast Agent for in Vivo X-Ray Computed Tomography Imaging. *J. Am. Chem. Soc.* **2007**, *129* (24), 7661–7665. https://doi.org/10.1021/ja071471p.

(45) Pandey, A.; Vighetto, V.; Di Marzio, N.; Ferraro, F.; Hirsch, M.; Ferrante, N.; Mitra, S.; Grattoni, A.; Filgueira, C. S. Gold Nanoparticles Radio-Sensitize and Reduce Cell Survival in Lewis Lung Carcinoma. *Nanomaterials* **2020**, *10* (9). https://doi.org/10.3390/nano10091717.

(46) Terracciano, R.; Zhang, A.; Simeral, M. L.; Demarchi, D.; Hafner, J. H.; Filgueira, C. S. Improvements in Gold Nanorod Biocompatibility with Sodium Dodecyl Sulfate Stabilization. *J. Nanotheranostics* **2021**, *2* (3), 157–173. https://doi.org/10.3390/jnt2030010.

(47) Cristini, V.; Koay, E.; Wang, Z. An Introduction to Physical Oncology: How Mechanistic Mathematical Modeling Can Improve Cancer Therapy Outcomes. *CRC Press* **2018**, *38* (1), 585–586.

FIGURE CAPTIONS

**Scheme 1.** Gold nanoparticles (GNPs) surface stabilized natively with citrate and surface passivated with poly(ethylene glycol) methyl ether thiol (PEG) and 1,2-dipalmitoyl-sn-glycero-3-phosphothioethanol (PTE) using conjugated thiol linkers.

**Figure 1.** GNP uptake is a function of surface passivation which affects cell viability in a cell line dependent manner. (A) Representative scanning transmission election microscopy images of LLC cells demonstrating uptake of (i) citrate-GNPs, (ii) PTE-GNPs, and (iii) PEG-GNPs. Elemental analysis performed with ICP-OES on (B) HeLa and (D) LLC cell pellets 24 h after treatment. MTT assays for (C) HeLa and (E) LLC cells treated and incubated for 24h with nascent and surface functionalized GNPs. (**$p < 0.005$ and ****$p < 0.0001$ by two-way ANOVA using Tukey's multiple comparisons test). All data in the figure are reported as mean ± s.e.m in triplicate.

**Figure 2.** GNP intratumoral biodistribution is dependent on surface passivation. (A) Photos of ex vivo tumors harvested 3, 6, and 9 days post-injection show gross evidence of differences in particle distribution. (B) Intratumoral gold quantified with elemental analysis (ICP-OES) 3, 6, and 9 days post-injection. (C) 3D reconstructions of tumors (pink) and particle distribution renderings (red) from μCT. (D) Intratumoral x-ray attenuation in Hounsfield units (HU) show contrast enhancement after injection on days 0, 3, 6, and 9 when compared with tumor baseline (pre-injection) imaging (dashed line, *$p < 0.05$, #$p < 0.05$). Pearson correlation was calculated between (B) ICP-OES and (D) μCT data, identifying agreement between results (††p

< 0.005). (E) Snapshots of the tumor model simulations taken at day 3, 6, and 9 post-injection show spatial distribution of the total GNPs (free + bound) for particles with Da values of 0.1, 0.01, and $1x10^{-5}$. These three values were featured as they qualitatively matched the experimental distribution patterns for the citrate, PTE, and PEG functionalized particles shown in A and C. The dashed white circle demarcates the tumor boundary. Color bar denotes NP concentration (mol $m^{-3}$). Scale bar = 1 cm. (F) Simulation quantification, where the graphs show the concentration of GNPs across the tumor diameter with -1 being the left edge of the tumor boundary and +1 being the right edge, obtained from model simulations. Red line indicates the concentration of NPs that are bound while the blue line is the concentration of freely diffusing NPs in the tumor. Note that the y-axes are in log scale.

**Figure 3.** Intratumoral quantification of particle zonal accumulation. (A) Schematic of methodology whereby the tumor was sectioned into 4 regions. Quantification of gold performed with elemental analysis on n = 4 tumors (B) 3 and (C) 6 days post-injection. Not visible areas in the boxes represent values of gold <0.5 %.

**Figure 4.** Effects of GNP treatment type on intratumoral zonal distribution. Groups include untreated, citrate-GNPs, PTE-GNPs, and PEG-GNPs treated tumor bearing mice. (A-D) In vivo CT slices of the tumors grown on the mouse flank, (E-H) ex vivo photos of the excised tumors sliced on a plane close to the injection point, and (I-L) H&E stain of the tumors (red boxes in E-H represent the area shown with 20x magnification in I-L, white arrows in J-K represent border zone between viable and necrotic tumor). Scale bar represents 200 μm.

FIGURES

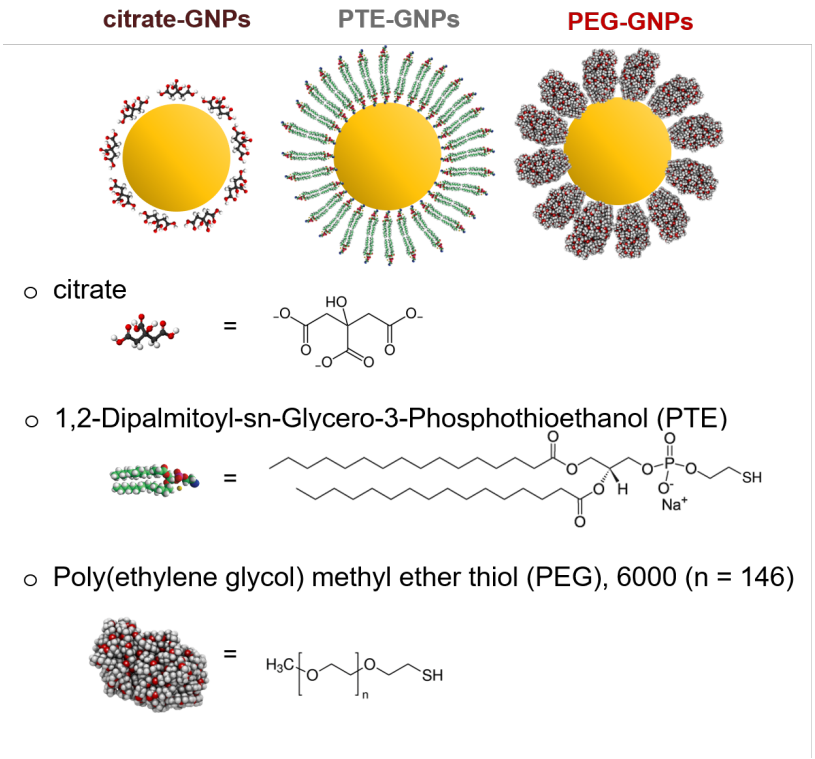


**Scheme 1.** Gold nanoparticles (GNPs) surface stabilized natively with citrate and surface passivated with poly(ethylene glycol) methyl ether thiol (PEG) and 1,2-dipalmitoyl-sn-glycero-3-phosphothioethanol (PTE) using conjugated thiol linkers.

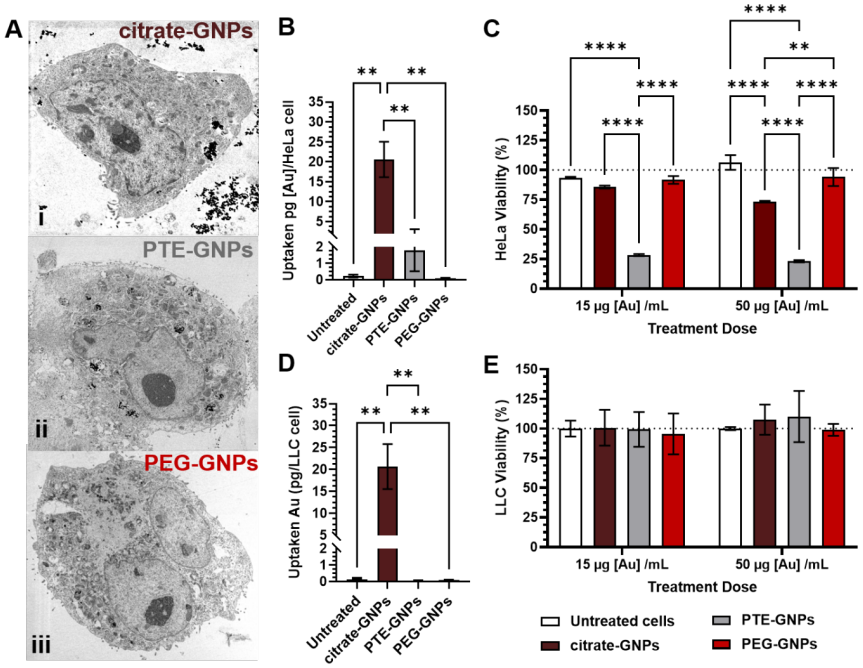


**Figure 1.** GNP uptake is a function of surface passivation which affects cell viability in a cell line dependent manner. (A) Representative scanning transmission election microscopy images of LLC cells demonstrating uptake of (i) citrate-GNPs, (ii) PTE-GNPs, and (iii) PEG-GNPs. Elemental analysis performed with ICP-OES on (B) HeLa and (D) LLC cell pellets 24 h after treatment. MTT assays for (C) HeLa and (E) LLC cells treated and incubated for 24h with nascent and surface functionalized GNPs. (**$p < 0.005$ and ****$p < 0.0001$ by two-way ANOVA using Tukey's multiple comparisons test). All data in the figure are reported as mean ± s.e.m in triplicate.

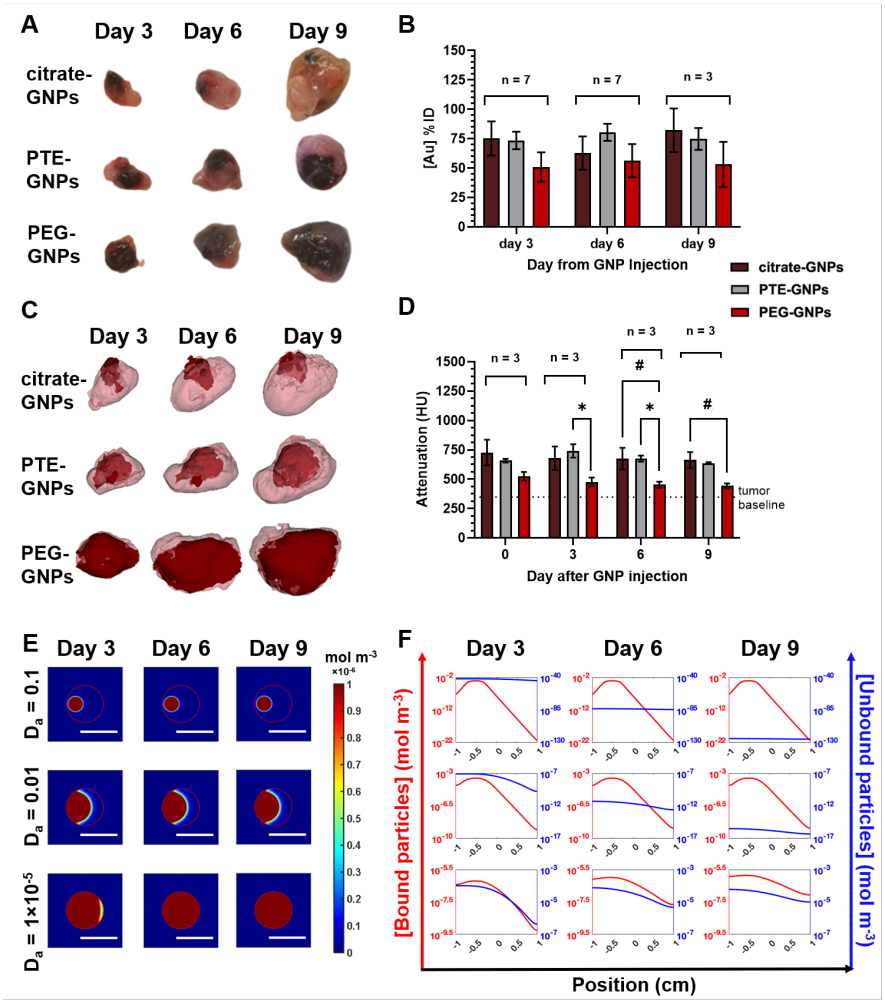


**Figure 2.** GNP intratumoral biodistribution is dependent on surface passivation. (A) Photos of ex vivo tumors harvested 3, 6, and 9 days post-injection show gross evidence of differences in particle distribution. (B) Intratumoral gold quantified with elemental analysis (ICP-OES) 3, 6, and 9 days post-injection. (C) 3D reconstructions of tumors (pink) and particle distribution renderings (red) from μCT. (D) Intratumoral x-ray attenuation in Hounsfield units (HU) show contrast enhancement after injection on days 0, 3, 6, and 9 when compared with tumor baseline (pre-injection) imaging (dashed line, *p <0.05, #p<0.05). Pearson correlation was

calculated between (B) ICP-OES and (D) μCT data, identifying agreement between results (††$p < 0.005$). (E) Snapshots of the tumor model simulations taken at day 3, 6, and 9 post-injection show spatial distribution of the total GNPs (free + bound) for particles with Da values of 0.1, 0.01, and $1x10^{-5}$. These three values were featured as they qualitatively matched the experimental distribution patterns for the citrate, PTE, and PEG functionalized particles shown in A and C. The dashed white circle demarcates the tumor boundary. Color bar denotes NP concentration (mol $m^{-3}$). Scale bar = 1 cm. (F) Simulation quantification, where the graphs show the concentration of GNPs across the tumor diameter with -1 being the left edge of the tumor boundary and +1 being the right edge, obtained from model simulations. Red line indicates the concentration of NPs that are bound while the blue line is the concentration of freely diffusing (unbound) NPs in the tumor. Note that the y-axes are in log scale.

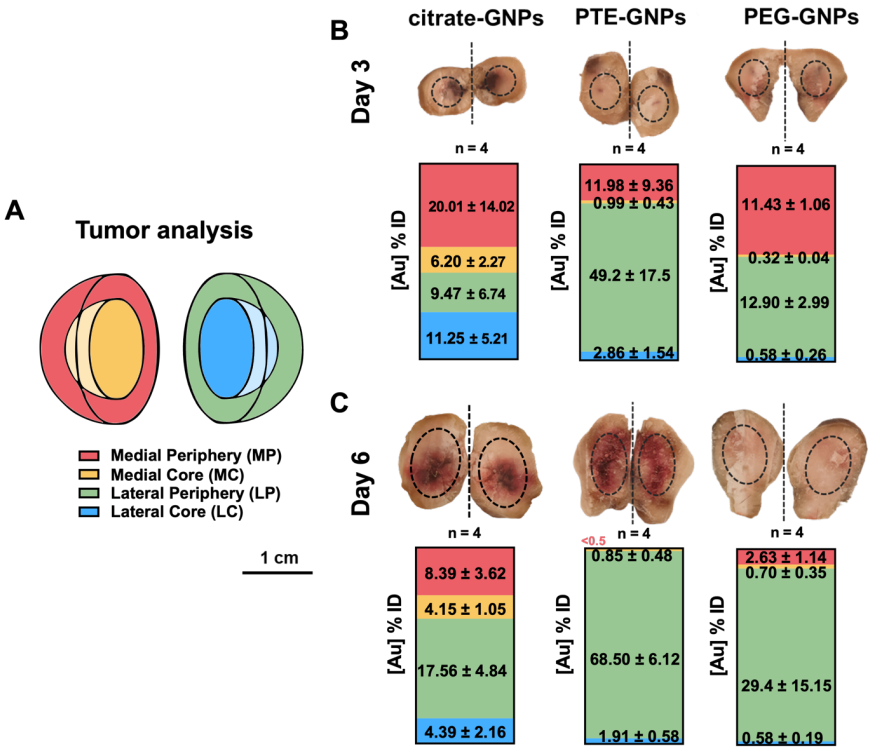


**Figure 3.** Intratumoral quantification of particle zonal accumulation. (A) Schematic of methodology whereby the tumor was sectioned into 4 regions. Quantification of gold performed with elemental analysis on n = 4 tumors (B) 3 and (C) 6 days post-injection. Not visible areas in the boxes represent values of gold <0.5 %.

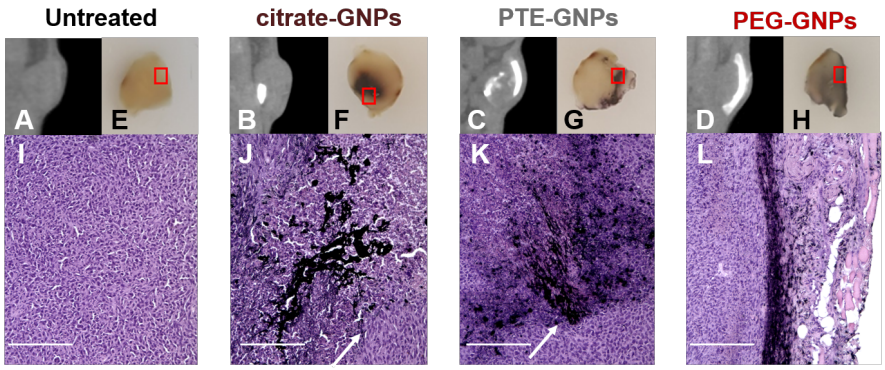


**Figure 4.** Effects of GNP treatment type on intratumoral zonal distribution. Groups include untreated, citrate-GNPs, PTE-GNPs, and PEG-GNPs treated tumor bearing mice. (A-D) In vivo CT slices of the tumors grown on the mouse flank, (E-H) ex vivo photos of the excised tumors sliced on a plane close to the injection point, and (I-L) H&E stain of the tumors (red boxes in E-H represent the area shown with 20x magnification in I-L, white arrows in J-K represent border zone between viable and necrotic tumor). Scale bar represents 200 μm.

TABLE OF CONTENTS

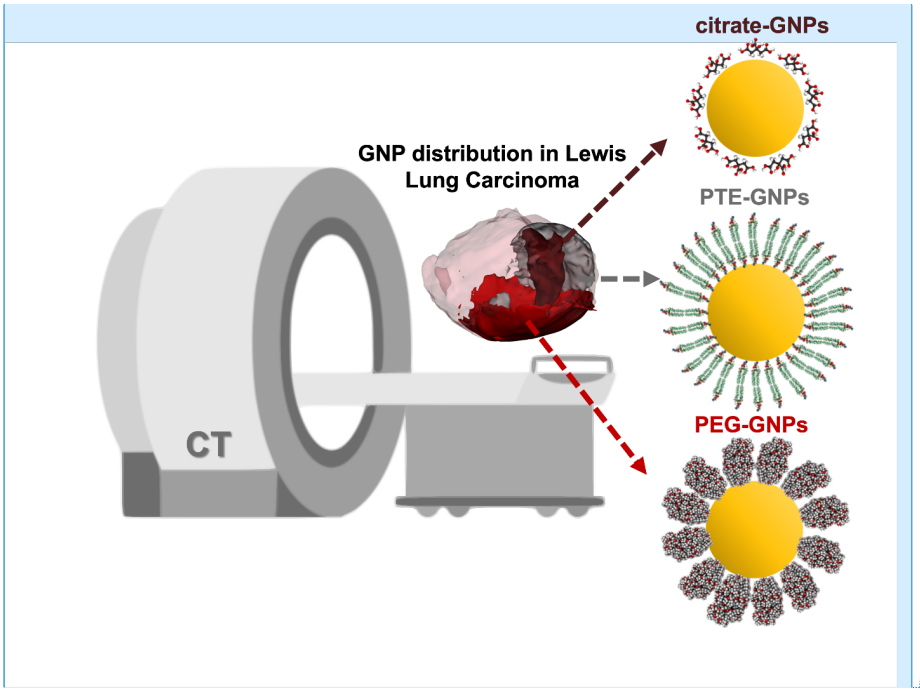


**Surface passivation of gold nanoparticles governs their intratumoral diffusion.** Computed tomography (CT) reveals different patterns of intratumoral diffusion of gold nanoparticles (GNPs) when their surface is functionalized with small molecules compared to their nascent, citrate stabilized form.

**Commented [GA5]:** A bit confusing bc it shows overlap of distribution in tumors among different surface modifications.